Progress In Electromagnetics Research, Vol. 177, 53–73, 2023

The Effects of Obscuration in Passive 3-D Millimeter-Wave Imaging for Human Security Screening

Xuelei Sun[1, *], Neil A. Salmon[2], Xiaodong Zhuge[1], and Jungang Miao[1]

Abstract—The possibility of near-field passive 3-D imaging using the aperture synthesis technique is theoretically proven and highlights the opportunity for imaging the entire human body by an antenna receiving array that surrounds the body. In these scenarios there will be partial obscuration of some regions of the body, by other parts of the body. This results in some receivers in the array being able to measure emission from certain parts of the body, while others are obscured from a measurement. A model is presented which enables the effects of obscuration to be assessed for planar-like, cylindrical-like, and concave-like regions of the human body. The effect the obscuration has on the spatial resolution of the imager is evaluated by examining the 3-D point spread function, as determined by a near-field aperture synthesis imaging algorithm. It is shown that over many areas of the human body, the Abbe microscope resolution of $\lambda/2$ (5 mm@30 GHz) in a direction transverse to the human body surface is achievable, an attractive proposition for security screening. However, the spatial resolution in a direction normal to the human body surface is shown to be close to λ (10 mm@30 GHz). In regions of greater obscuration, such as in the armpits, the resolution may fall to λ (10 mm@30 GHz) and 5λ (50 mm@30 GHz) in the directions transverse and normal to the human body surface, respectively. It is also shown by simulation using a human body solid model and the 3-D aperture synthesis imaging algorithm how the image quality changes with the number of receiving antennas.

1. INTRODUCTION

Millimeter-wave (mm-wave) imaging is emerging as an effective commercial security screening technique for the detection of concealed weapons and contraband on persons [1–3]. Currently, systems fall into two basic categories, the first being active and the second being passive. Active systems are a type of radar, generating an image by illuminating a subject with man-made (artificial) coherent radiation and measuring the reflections. Passive systems are a type of radiometer, generating their images by measuring the radiometric (or thermal) emission from the subject and the reflections from the natural radiation in their environment.

The traditional 2-D passive mm-wave (PMMW) imaging systems show advantages of moderate system cost, video-rate imaging [4–6], and high image contrast in outdoor scenarios [7, 8] due to the low levels of natural environmental illumination from the sky. However, for indoor scenarios, the image contrast is low, making the discrimination between the human body and the concealed object more challenging [4, 9]. To raise the contrast in these images, illumination from sources of (incoherent) radiation was used, with they emulating the properties of thermal radiation in outdoor environments [10, 11]. This helped the detection of concealed metal objects, but non-metallic objects remained difficult to detect, as shown in Figure 1. Thus, the detection and recognition of non-metallic threats and contraband in indoor scenarios are still very challenging.

Received 13 January 2023, Accepted 30 May 2023, Scheduled 4 June 2023
* Corresponding author: Xuelei Sun (xlsun@buaa.edu.cn).
[1] School of Electronics and Information Engineering, Beihang University, Beijing, China. [2] MMW Sensors Ltd, UK.

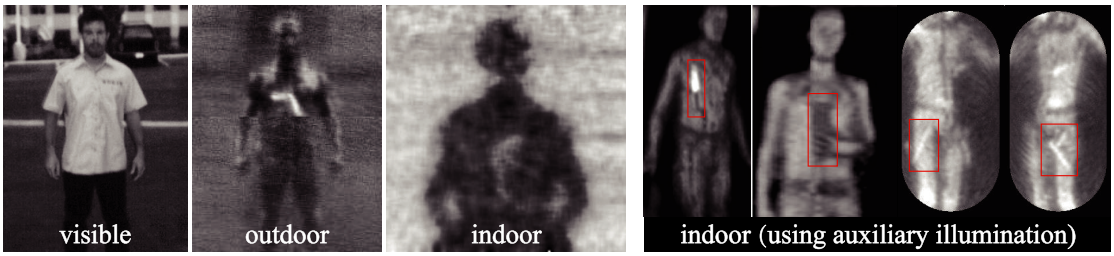

(a) (b)

Figure 1. Experimental results for PMMW human security screening from the open literature: (a) comparison of the visible radiation image, the outdoor PMMW image, and the indoor PMMW image of a man carrying a metal gun [4]; (b) indoor PMMW images of a man carrying a metal knife [11], an explosive simulant [11], a ceramic knife [10], and a gun [10], using auxiliary (incoherent) illumination radiation sources.

A possible solution to detecting and recognising contraband with a PMMW imager is to exploit the radio astronomy technique of aperture synthesis [12] in the near-field. Aperture synthesis imaging systems have already been developed and capable of creating imagery in the near-field [7, 13, 14]. However, these systems do not yet fully exploit the potential of the aperture synthesis technique. This is because the antenna array is not close enough to the subject to image simultaneously the front and sides of the body, a scenario in which the spatial resolution of the measurement becomes of the order of the wavelength. Furthermore, operation in such a near-field environment would enable the 3-D shape of the object (a 3-D image) to be formed and viewed from multiple perspectives. Together with the surface brightness temperatures, this would enable detection and recognition of threat objects on the human body. This technique could go some way to ameliorating the deleterious effects of low image contrast in indoor environments.

The feasibility of PMMW 3-D imaging has been theoretically proven using the aperture synthesis technique [15–18]. The principle of this technique is based on the generalized 3-D van Cittert-Zernike (VCZ) theorem [18, 19]. Accordingly, the 3-D brightness temperature of an object can be reconstructed by the 3-D Inverse Fourier Transform (3-D IFT) of a calibrated visibility function. The visibility function is formed from the cross-correlations of electric fields measured from pairs of receivers. It is calibrated in the near-field by putting a phase centre in the centre of the 3-D field-of-view (FOV), whereas for 2-D radio astronomy this is normally put at infinity [18, 20]. Numerical simulations indicate that if a subject is surrounded by receivers, the Abbe microscope spatial resolution for incoherent imaging [21] of half a wavelength may be achieved in 3-D, which may be improved upon if auxiliary information is provided [15, 20].

Practical limitations in the implementation of 3-D aperture synthesis may arise when parts of the human body are obscured from measurement by other parts of the body. For example, the arms may obscure some receivers from measuring parts of the sides of the body. Likewise, one leg of the body may obscure the inner of the other leg. In the previous study of passive 3-D imaging [18], the radiation from a point radiator was assumed to be measured by all receivers, so these obscuration effects were not evaluated. In a real situation, not all receivers will be able to view all regions of the human body simultaneously. Even if omnidirectional (0 dBi gain) antennas are used, and there are no body parts obscuring other regions of the body, any surface can only be observed from a maximum solid angle of 2π steradians. Realistic antennas for an imaging system will have gain (> 0 dBi), meaning that regions of the body will only be measured by pairs of antennas over a solid angle of less than 2π steradians. The effect of this will be a vignetting of the image, whereby the spatial resolution in certain regions of the human body may be degraded from the optimal half-wavelength resolution.

The objective of this study is to analyze the theoretically achievable spatial resolution in images formed by the 3-D aperture synthesis technique in the application of passive human security screening, taking the obscuration effects into consideration. The main contributions of this paper can be summarized as follows:

(i) A model of obscuration effects in 3-D passive aperture synthesis imaging is presented, and the

Common-space Solid Angle is proposed to describe the degree of non-obscuration of different regions of the human body.

(ii) The point spread function (PSF), which is a function of the object imaged, is calculated to show how the obscuration impacts the imaging spatial resolution of different regions of the body.

(iii) It is verified that the obscuration effects will mainly affect the imaging spatial resolution in the direction normal to the human body surface.

The remainder of this paper is organized as follows. Section 2 describes the fundamentals of passive 3-D aperture synthesis imaging. In Section 3, the phenomenon of the obscuration effects is discussed and modeled. Section 4 analyzes the impact of the obscuration effects on spatial resolution using the proposed model. In Section 5, a human body model is built and used to analyze the spatial resolution in the imagery of several locations on the human body. In Section 6, the impact of the numbers of the antenna elements and future work are discussed. Section 7 concludes the paper.

2. 3-D APERTURE SYNTHESIS IMAGING FUNDAMENTALS

The configuration of a two-element interferometer is depicted in Figure 2. The receiving antennas A_1 and A_2 are located at (x_1, y_1, z_1) and (x_2, y_2, z_2), respectively. The extended 3-D object has a brightness temperature distribution of $T(x, y, z)$, whereby the individual radiators of the object are necessarily independent radiators [22], a fundamental property of thermal radiation. The volume element dV denotes the point radiator located on the surface of the object. Only the independent radiators located on the surface of the object can contribute to the radiation field of the object. The unit vector normal to the object surface is denoted by $\widehat{n}$, and the unit direction vector pointing from the radiator to the antenna is $\widehat{r}_i$, where $i = 1, 2$ designates the receiving antenna, and θ_i is the angle between $\widehat{n}$ and $\widehat{r}_i$.

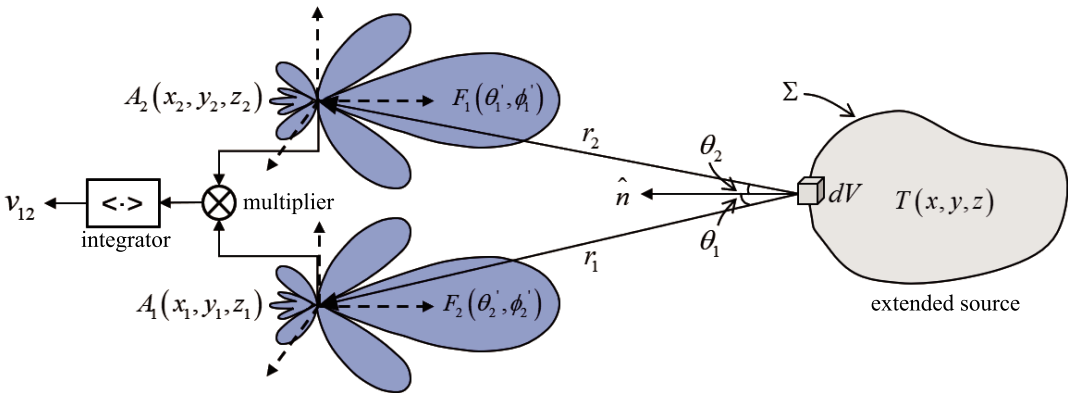

Figure 2. A schematic showing an extended source (object to be imaged) having a brightness temperature $T(x, y, z)$, two measurement antennas A_1, A_2, a conjugate multiplier and an integrator of a 3-D aperture synthesis imager in a Cartesian coordinate system. The two channels by themselves constitute the classic two-element interferometer from radio astronomy. This is a sample figure.

In a practical imaging system, the antenna radiation pattern $F_i(\theta_i', \phi_i')$ and the receiver impulse response $H_i(f)$ should be taken into consideration. According to [19, 23, 24], the formula of the output of the two-element interferometer, which constitutes one component of the visibility function from an array of receivers, is given by

$$v_{12}(\tau) = K \iiint_{\Sigma} \frac{\cos(\theta_1)\cos(\theta_2)}{r_1 r_2} T(x, y, z) \left|F_1\left(\theta_1', \phi_1'\right)\right| \left|F_2\left(\theta_2', \phi_2'\right)\right| \gamma_{\widetilde{A}}(\tau) \exp\left(j2\pi f_{\mathrm{IF}}\tau\right) dV \tag{1}$$

where

$$K = \frac{k_B \alpha_1 \alpha_2 \sqrt{B_1 B_2}}{\lambda_0^2}$$

is a constant coefficient of the system. k_B is the Boltzmann's constant. α_i is the voltage gain of the receiver channel. B_i is the filter equivalent noise bandwidth of the receiver. f_{IF} represents the intermediate frequency (IF) of the receiver. λ_0 is the wavelength corresponding to the central frequency f_{IF}. Σ represents the outward surface of the object. The range between the radiator and the ith receiving antenna can be calculated by

$$r_i|_{i=1,2} = \sqrt{(x_i - x)^2 + (y_i - y)^2 + (z_i - z)^2}$$

$\gamma_{\widetilde{A}}(\tau)$ is the fringe-washing function. $\tau = (r_2 - r_1)/c$, where c is the velocity of light.

Noteworthy, the integral domain in (1) is the surface of the object, and the values of $\cos(\theta_1)$ and $\cos(\theta_2)$ are partially dependent on the geometry of the object. For simplicity, the complex cross-correlation $v_{12}(\tau)$ can be rewritten as

$$v_{12}(\tau) = K \iiint_{\Sigma} \frac{1}{r_1 r_2} T'(x,y,z)\, \gamma_{\widetilde{A}}(\tau) \exp(j2\pi f_{\mathrm{IF}}\tau)\, dV \tag{2}$$

where

$$T'(x,y,z) = \cos(\theta_1)\cos(\theta_2) \left|F_1\left(\theta_1', \phi_1'\right)\right| \left|F_2\left(\theta_2', \phi_2'\right)\right| T(x,y,z)$$

is defined as the modified brightness temperature [2]. Ideally, if the radio frequency passband of the receiver channel is narrow, the fringe-washing function $\gamma_{\widetilde{A}}(\tau)$ approximates to unity, which simplifies the calculation [23].

The visibility function (2) is a nonlinear equation, which means that a closed-form of the modified brightness temperature has no solution. However, under the far-field approximation, the visibility function reduces to a linear equation [25]

$$v_{FF}(u,v,w) \propto \iiint_{\Sigma} T'(x,y,z) \exp\left[-j2\pi(ux + vy + wz)\right] dxdydz \tag{3}$$

where the parameters

$$\mu = \frac{x_j - x_k}{\lambda_{\mathrm{IF}} R} \quad \upsilon = \frac{y_j - y_k}{\lambda_{\mathrm{IF}} R} \quad \omega = \frac{z_j - z_k}{\lambda_{\mathrm{IF}} R}$$

are known as the Cartesian coordinate spatial frequency components. The average distance between the receiving antennas and the extended object is given by R, where the coordinate indices $i = 1, 2$ are replaced by j and k, respectively, to represent a two-element interferometer comprising antennas j and k from the full array. Thus, under far-field conditions, the modified brightness temperature can be reconstructed by a 3-D IFT of the visibility function.

For short-range imaging, the distance between the regions of the body being screened and the receiver antennas is close to the size of the human body. Although the visibility function can be transformed to the far-field by the electrical refocusing technique [18, 26], the Fourier transformation relationship between brightness temperature and the visibility function is only valid in a relativity small region around the focusing center [17]. As a result, the maximum unambiguous imaging region, which can be defined as the FOV, is relatively small compared to the human body. Thus, the spatial resolution far away from the focusing center is poor.

To obtain a larger FOV and better imaging quality, a near-field focusing algorithm (NFA) [27] is used in this study. For each voxel in the FOV, the modified brightness temperature can be calculated by

$$T'(x,y,z) \propto \sum_{k=1}^{N} \sum_{j=1}^{N} v_{kj} \exp\left(j2\pi f_{\mathrm{IF}} \frac{r_k - r_j}{c}\right) \tag{4}$$

where N is the number of the receiving antennas. The concept here is derived from the principles of a phased array receiver. The complex cross-correlation of a pair of receivers is a superposition of autocorrelations generated by each independent radiator in the FOV. By compensating for the range difference between the focus point and the two receiving antennas, the phase of the autocorrelation from the radiator at the focus point will be set to zero. Phases of the autocorrelations from all other radiators,

away from the focus point, will be nonzero. By adding together the complex cross-correlations from all pairs of receivers, the zero phase components will be enhanced, whilst the out-of-phase components will be attenuated. The summation in the equation therefore generates a phase corrected (modified) brightness temperature proportional to the radiation temperature at the focus point.

3. MODELING OBSCURATION EFFECT

In the previous study, it was assumed that all of the receiving antennas could receive electromagnetic radiation from each radiator on the human body. However, in a practical passive imaging system, obscuration will prevent electromagnetic radiation radiated from each part of the human body from being received by all receiving antennas surrounding the human body.

From the antenna perspective, the receiving antenna at any position can only receive radiation from part of the human body. Thus, for an arbitrary receiving antenna, the human body surface can be divided into an observed region and a hidden region. As shown in Figures 3(a) and (b), the observed region and hidden region are different for antennas at different locations. Each antenna can only receive emission from those radiators in the observed region. The radiated signals of different radiators on the human body are spatially incoherent. Therefore, only radiators located in the common observed region of both antennas of a pair will generate a cross-correlation. As shown in Figure 3(c), the common observed region of a two-element interferometer is the overlap of the observed regions of each of the two antennas.

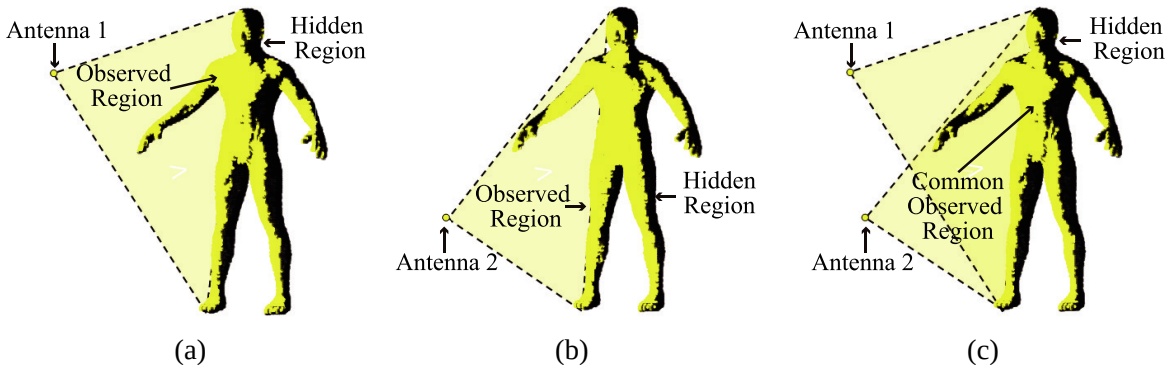

Figure 3. The obscuration effects: (a) the observed region and the hidden region for receiving Antenna 1; (b) the observed region and the hidden region for receiving Antenna 2; (c) the common observed region of Antenna 1 and Antenna 2 is the overlap region of their respective observed regions.

From the radiator perspective, the full 4π steradian of space surrounding a single radiator can also be divided into an observed space and a hidden space. Only the antennas located in the observed space of the single radiator can receive the emitted signals. These antennas are referred to as effective antennas and can generate a cross-correlation. Others are referred to as obscured antennas, which are located in the hidden space and obscured by other opaque objects or surfaces. If the solid angle of observed space of a single point radiator is 4π, then the corresponding solid angle of the hidden space is zero. However, for an independent radiator on the human body surface, due to the obscuration from other parts of the human body, the solid angle of antennas that can receive the signals emitted from the independent radiator is no greater than 2π. Thus, there comes a hypothesis that the imaging spatial resolution of a point located on an extended object is related to the corresponding observed space solid angle of that point. Therefore, the degree of obscuration effects can be quantitatively described by the size of the observed space solid angle.

In an actual imaging scenario, the observed space of a point located on the surface of an extended object may be irregular. For simplicity, a simplified obscuration model shown in Figure 4 is proposed to study the deterioration of spatial resolution with the observed space solid angle. A point radiator is placed in the center of a spherical array having equally spaced antennas. The observed space of the

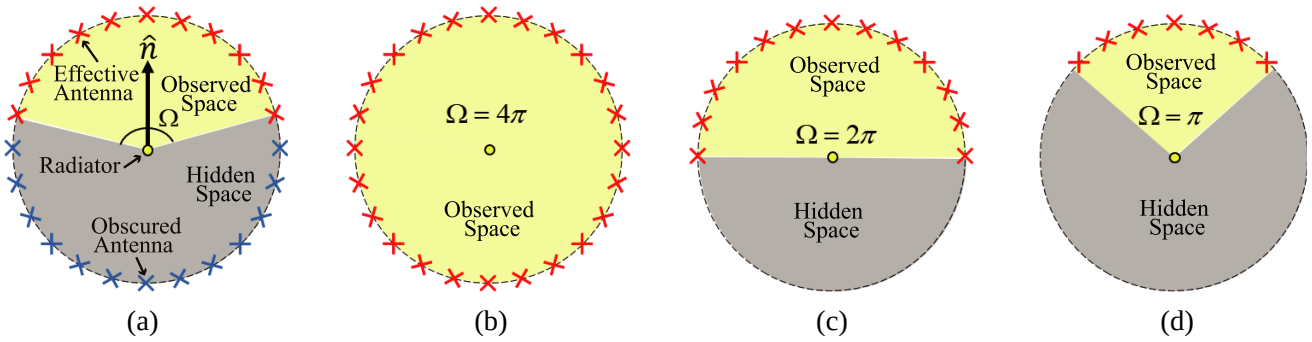

Figure 4. (a) The simplified obscuration model. The space around a point radiator can be divided into the observed space and the hidden space. Other models having a CSA (Ω) of: (b) 4π (the ideal case, with no obscuration, only realistic for a point source); (c) 2π (the planar- and cylindrical-like body structures); (d) π (the concave structures of the body).

point radiator is assumed to be cone shaped, with the point radiator as its vertex. The vertex solid angle of the cone is defined as the Common-space Solid Angle (CSA). The center axis of the observed space is assumed to be the normal direction ($\widehat{n}$) of the point radiator. Under this condition, the CSA (Ω) can be estimated by

$$\Omega \approx \frac{M}{N} \cdot 4\pi \tag{5}$$

where M is the number of effective antennas, and N represents the number of all antennas in the array. If the Z-axis direction is set to be the normal direction of the radiation source, then the CSA of different sizes (e.g., 4π, 2π, and π) can be easily obtained by changing the extent of the sphere covered by the effective antennas, as illustrated in Figures 4(b), (c), and (d).

The surfaces of the human body can be classified from their geometrical form into three broad structure types, these being planar-like, cylindrical-like, and concave-like. As shown in Figure 5, most of the independent radiators on the human body are distributed on planar-like structures, for example, on the chest, the abdomen, and the back. The arms and legs are cylindrical-like structures. A few areas, such as the armpits and between legs, are concave-like structures. The CSA of these typical structures

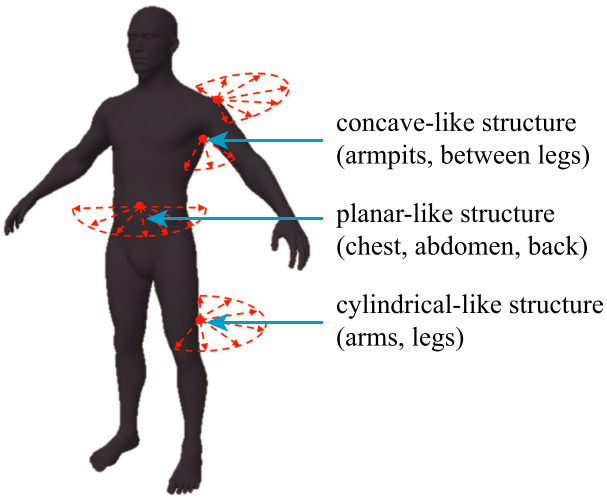

Figure 5. The surfaces of the human body can be classified from their geometrical form into three broad structure types, these being, concave-like, planar-like, and cylindrical-like.

are assumed to be:

$$\Omega \begin{cases} \approx 2\pi, & \text{for the planar-like structures;} \\ \approx 2\pi, & \text{for the cylindrical-like structures;} \\ < 2\pi, & \text{for the concave-like structures.} \end{cases}$$

Compared with the ideal case of no obscuration, the CSA of a point radiator on the human body surface reduces from 4π to 2π; half of the volume falls in the observed space, whilst the other half is in the hidden space. This may result in deterioration of the spatial resolution.

4. SPATIAL RESOLUTION ANALYSIS

In this section, the simplified obscuration model proposed in Section 3 is used to analyze the impact of the obscuration effects on PMMW 3-D imaging. The spatial resolution is analyzed by calculating the half-power beamwidth (HPBW) of the PSF created by the effective antennas in the array. Although the algorithm from Section 2 can be used to generate the image from an arbitrary shaped antenna array around the subject, for the convenience of programming a spherically shaped array has been used in the simulations. In addition, another benefit of using a spherically shaped array is that it can adequately sample the 4π steradian space surrounding the point radiator. The receiving antennas are evenly placed over the surface, forming a Fibonacci lattice [28], whereby the antenna coordinates (x_i, y_i, z_i) of the ith antenna in an N-element spherical array with a diameter of D are given by

$$z_i = \frac{1}{2} D \left[(2i-1)/N - 1 \right] \tag{6a}$$

$$x_i = \frac{1}{2} D \left[\sqrt{1 - {z_i}^2} \cdot \cos(2\pi i \phi) \right] \tag{6b}$$

$$y_i = \frac{1}{2} D \left[\sqrt{1 - {z_i}^2} \cdot \sin(2\pi i \phi) \right] \tag{6c}$$

where

$$\phi = \left(\sqrt{5} - 1 \right) / 2 \approx 0.618$$

is the golden section ratio. A Fibonacci lattice is employed as this minimizes the distances between nearest neighbor antennas, which has the effect of minimizing aliasing.

Figure 6 shows the topology of a 500-element antenna array with a diameter of 3 meters, with the coordinate origin located at the center of the spherical array. A figure of 500 elements has been chosen as this is something that could be realised now in a proof-of-concept imager, without undue cost, whilst a smaller number of antennas may suffer problems associated with aliasing [18]. The receiving antennas

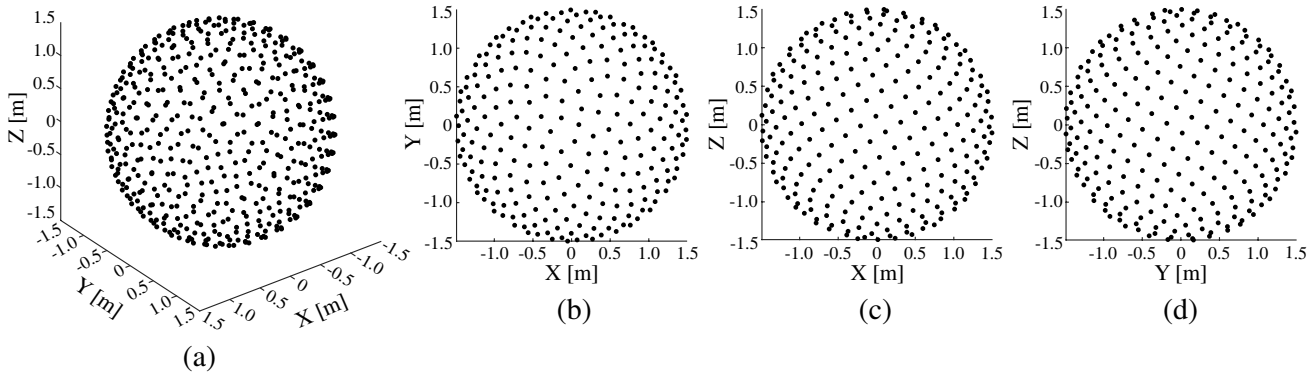

Figure 6. The spherically shaped array used in the simulations has a diameter of 3 meters and has 500 antennas spaced evenly over its surface, shown here as: (a) a perspective view; (b) view from above, looking down the Z-axis; (c) side view, looking along the Y-axis; (d) side view, looking along the X-axis.

are assumed to be omnidirectional with a gain of 0 dBi in all directions. A simulation frequency of 30 GHz was chosen, as this is expected to give good spatial resolution and in a spectral region where most clothing is almost completely transparent.

4.1. The Ideal Case, No Obscuration

In the ideal case, the Dirac delta function is used as the point radiator. The CSA of the point radiator is 4π, as nothing prevents the radiator from emitting in all directions. The PSF of the ideal imaging system is defined as the delta function response from this point radiator, which, according to Section 2, can be approximated by

$$\mathrm{PSF} = K \sum_{k=1}^{N} \sum_{j=1}^{N} \left[\iiint_{\Sigma} \frac{1}{r_k r_j} \delta\left(x - x_0, y - y_0, z - z_0\right) \exp\left(j2\pi f \frac{r_j - r_k}{c}\right) dV \right] \exp\left(j2\pi f \frac{r_k - r_j}{c}\right) \quad (7)$$

where $\delta(x, y, z)$ is the Dirac delta function, and (x_0, y_0, z_0) represents the position of the point radiator in Cartesian coordinates. From the property of the Dirac delta function, (7) reduces to

$$\mathrm{PSF}\left(x, y, z, x_0, y_0, z_0\right) \propto \sum_{k=1}^{N} \sum_{j=1}^{N} \frac{1}{r_{k0} r_{j0}} \exp\left[j2\pi f \frac{(r_{j0} - r_j) - (r_{k0} - r_k)}{c}\right] \quad (8)$$

where

$$r_{i0}|_{i=k,j} = \sqrt{(x_i - x_0)^2 + (y_i - y_0)^2 + (z_i - z_0)^2}$$

is the distance between the ith receiver and the point radiator. It is observed that the PSF of this imaging system is space-variant because the far-field condition cannot be satisfied at all locations within the spherical array of antennas. Due to the symmetry of the spherically shaped array, the PSFs of positions equidistant from the coordinate origin are equivalent. For simplicity, a point radiator is placed on the Z-axis to explore the spatial resolution inside the spherical array.

Figure 7 illustrates the predicted PSFs at the positions (0,0,0) and (0,0,1), these being the centre and the edge of the spherical array of antennas, respectively, for the ideal ($\Omega = 4\pi$) condition. The PSF

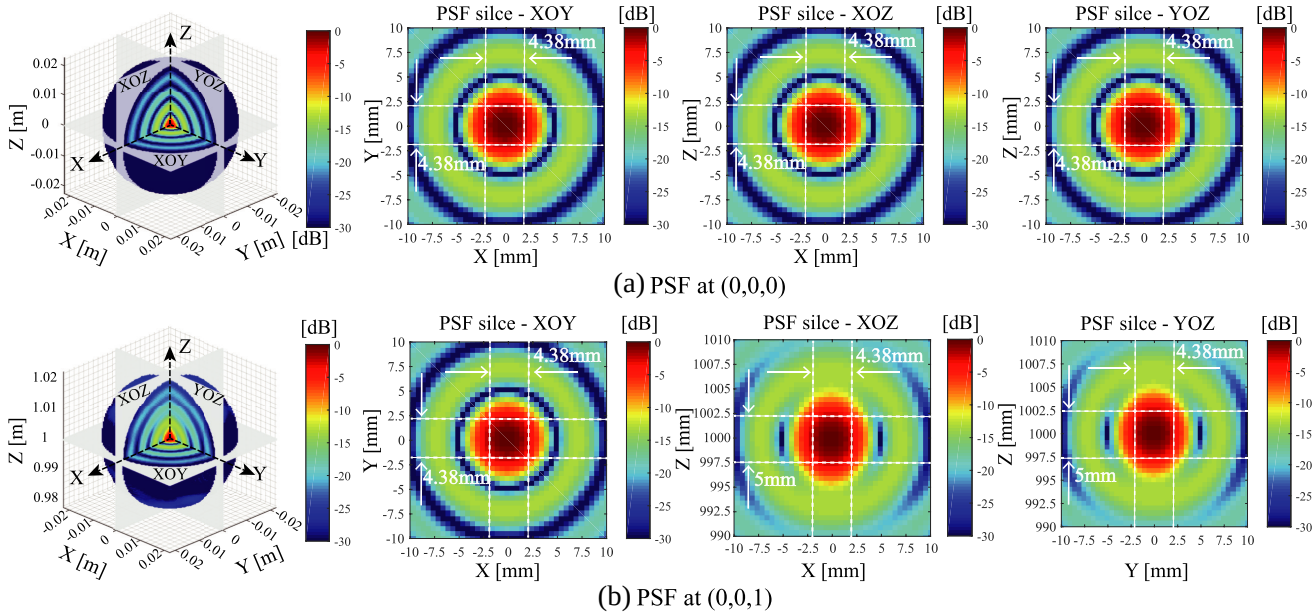

Figure 7. The ideal ($\Omega = 4\pi$) PSF at the location (a) (0,0,0) and (b) (0,0,1) in the 3-D imager field of regard, illustrating: a 3-D perspective view and slices through: the "XOY" plane; the 'XOZ" plane; the "YOZ" plane.

slices on the "XOY", "XOZ", and "YOZ" planes are shown for clarity in these figures. Compared with the PSF at the coordinate origin (0,0,0), that at the edge of the sphere, the coordinate (0,0,1), is slightly broadened in the Z-axis direction. It is observed that the HPBW of the PSF in the X- and Y-axes directions are the same, having a value of 4.38 mm. However, in the direction of the Z-axis, the HPBW increases to 5 mm as the position of the radiator approaches (0,0,1). This means that as the edge of the sphere of antennas is approached, the spatial resolution in the direction perpendicular to the sphere surface is degraded by just 0.62 mm. In conclusion, for the 500-element spherically shaped array with a diameter of 3 meters, the theoretical spatial resolution (without obscuration) within the sphere of antennas can be assumed to be $\lambda/2$ (5 mm@30 GHz).

4.2. Impact of Obscuration Effects

The spatial resolution is now analysed to include the effects of obscuration, using the simplified model shown in Figure 4, where the Z-axis is now fixed in the direction normal to the point radiator. Different degrees of obscuration of a point radiator located in the center of the array can be simulated by removing some of the receiving antennas from the spherical array. Then, the situations of $\Omega = 4\pi$ (the ideal case of no obscuration as a comparison), 2π, and π can be obtained, as illustrated in Figure 8. The corresponding PSF slices on the XOY, XOZ, and YOZ planes for the range of CSAs are then

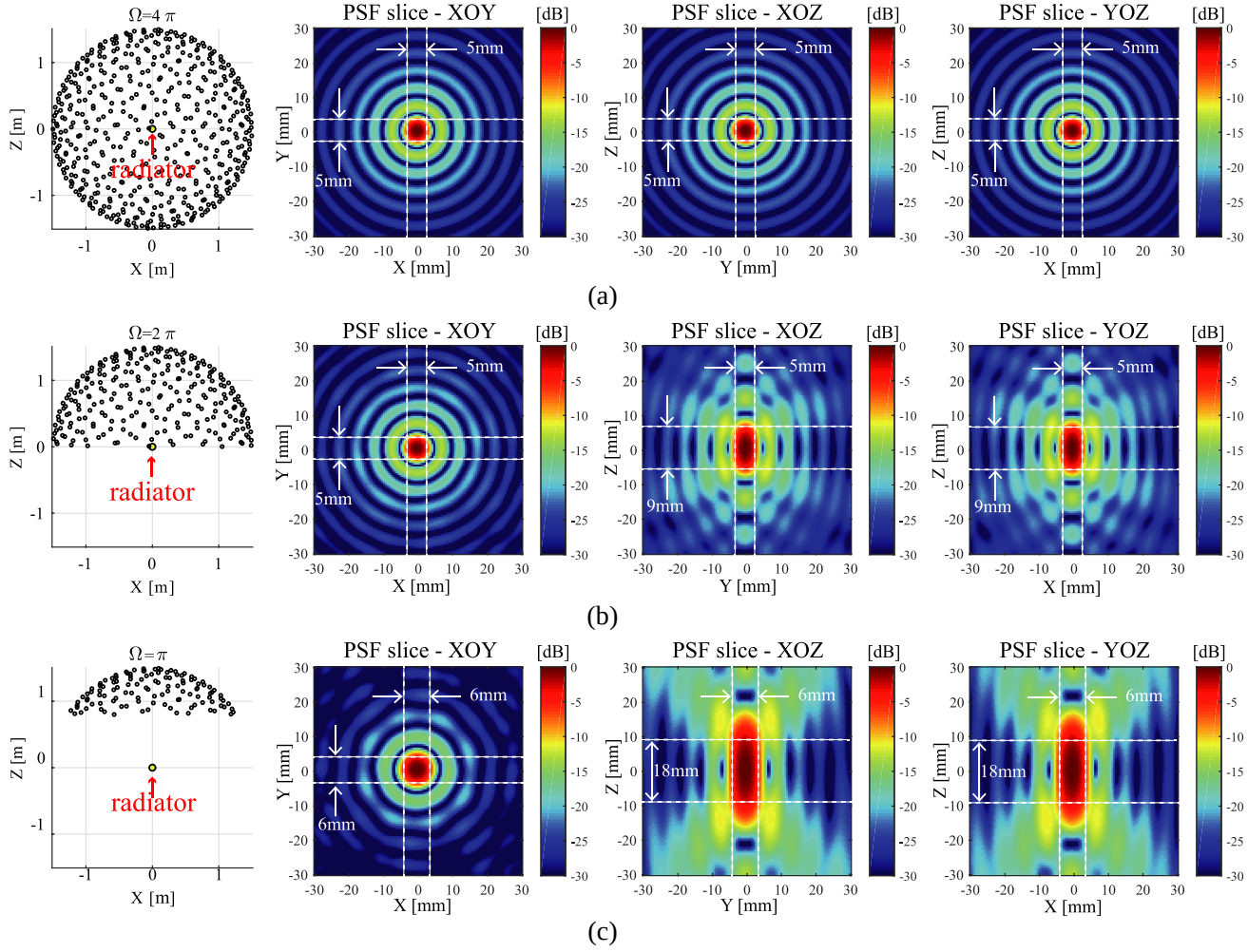

Figure 8. A depiction of the simulation model showing how the CSA of the array is varied, taking values of: (a) $\Omega = 4\pi$, (b) $\Omega = 2\pi$, and (c) $\Omega = \pi$, with the corresponding PSF slices on the XOY, XOZ, and YOZ planes.

calculated and also shown in Figure 8. It can be observed from these results that the PSF beamwidth is significantly broadened in the Z-axis direction as the CSA is reduced. However, the effects on the PSF in the X- and Y-axis directions is far less.

From these plots, the variation of the HPBW in the directions of the three axes as a function of the CSA can be determined, and this is shown in Figure 9. These results show that the deterioration of the HPBW in the normal direction (the Z-axis) is quite large as the CSA is reduced to $\pi/2$, whilst the HPBW changes in the transverse directions (X- and Y-axes) are much smaller. In addition, the HPBW, in other words, the spatial resolution in the transverse directions (X- and Y-axes) is consistent with the Abbe microscope spatial resolution limit [21].

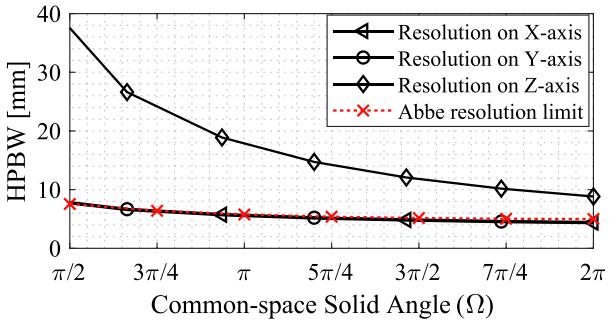

Figure 9. The variation of the HPBW of the PSF with the CSA for the antenna arrays illustrated in Figure 8 for a radiation frequency of 30 GHz. The spatial resolution along the X- and Y-axes is close to $\lambda/2$ and the along the Z-axis it approaches $\sim 5\lambda$ for small solid angles.

As discussed in Section 3, the CSA of the majority of regions on the human body is about 2π. It is shown in Figure 9 that the spatial resolution for $\Omega = 2\pi$ is approximately 1λ (10 mm@30 GHz) and $\lambda/2$ (5 mm@30 GHz) for the normal and the transverse directions, respectively. However, for areas like the armpits and between legs, where the CSAs are smaller than 2π, the achievable spatial resolution is in the range 1λ to 5λ (10 mm–50 mm@30 GHz) and $\lambda/2$ to λ (5 mm–10 mm@30 GHz) for normal and transverse directions, respectively. That means the transverse spatial resolutions are optimal ($\leq \lambda$) for all structural regions of the human body, whilst the normal spatial resolutions are not quite so favourable for regions of the body where surfaces are concave.

5. SIMULATION VALIDATION

In this section, a human body model is established to demonstrate the impact of the obscuration effects on 3-D imaging of the human body. The spherically shaped array is used as the imager. Each antenna is assumed to be omnidirection, in other words, it has a 0 dBi gain. The human body model with a height of 1.8 meters is generated using the open-source software "MakeHuman" [29] and is placed in the center of the imager. Simulations are performed at a radiation frequency of 30 GHz.

5.1. Spatial Resolution of Several Typical Locations on the Human Body Surface

The spatial resolution at several locations on the human body, shown in Figure 10(a), is analyzed. The selected locations are: the shoulder (point A) and the chest (point B), which are situated on the planar-like structures; the outer side of the upper arm (point C) and the front side of the thigh (point D), which are on the cylindrical-like structures; the armpits (point E), the inner side of the upper arm (point F), and between legs (point G), which are situated on the concave-like structures of the human body. It is assumed that an independent radiator is placed at one of the selected positions. The obscuration of other parts of the human body is taken into consideration to determine the effective antennas. These effective antennas are then used to generate the visibility function, which is then used to calculate the PSF using the algorithm described in Section 2. The HPBW of the PSF represents the spatial resolution when imaging the above specified regions of the human body.

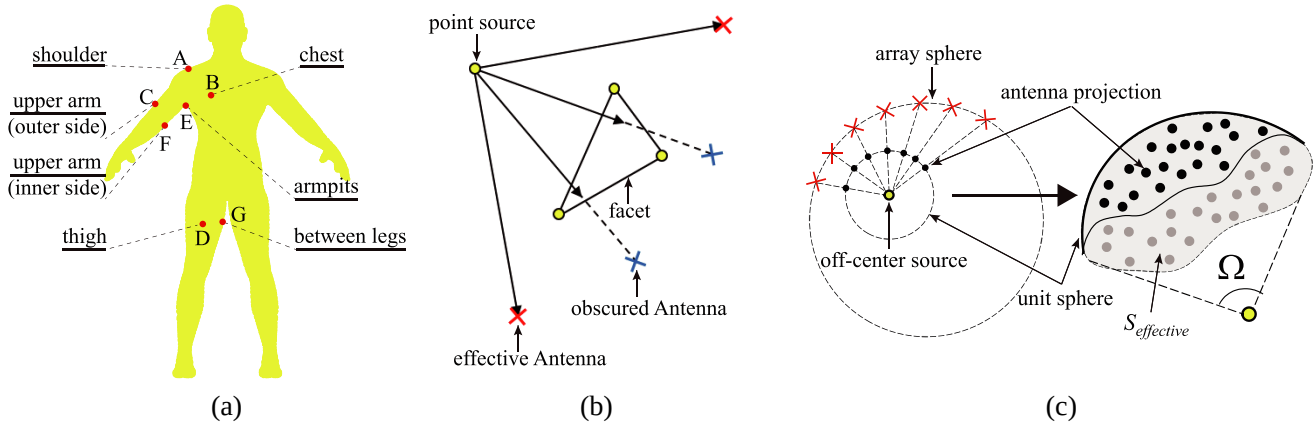

Figure 10. (a) Locations selected to calculate the spatial resolution. (b) Schematic illustrating ray-tracing used to determine which antennas will form the set of effective antennas. If a ray does not intersect any of the facets of the human body, there is no obscuration and the ray then continues its path to an effective antenna. If there is an intersection of the ray, this means an obscuration has occurred. (c) Schematic illustrating how the CSA is computed for an off-center source.

The effective antennas that can receive radiation from the point radiator are calculated via a ray-tracing technique [30]. Important assumptions and steps in the calculation are: 1) there are a finite number of rays starting from the point radiator and ending at each antenna element in the array; 2) the intersection point of each ray at each facet of the human body model is calculated; 3) rays propagate in straight lines. The latter assumption is valid as the propagation between the antenna element phase center and the human body is only through air, for which the refractive index is so close to unity that effectively no refraction takes place, which would otherwise deviate the beam from a straight line. Furthermore, the distance between these two points is many wavelengths, so near-field inductive antenna effects can be neglected. As illustrated in Figure 10(b), if the ray taken from a point radiator on the human body to the receiving antenna does not intersect any of the other facets on the human body, then that antenna is deemed an effective antenna. Stepping through all the point radiators for particular locations of the body, some antennas will never intersect a ray. These antennas are then referred to as obscured antennas. Data from obscured antennas are excluded from the calculation of the visibility function. The spherically shaped array shown in Figure 6 is used as the imager to analyze the imaging spatial resolution.

The CSA (Ω) can be estimated according to the distribution of the effective antennas. At this time, Equation (5) is no longer suitable for estimating the CSA, as the point radiator is no longer at the center of the imager. Under these conditions, an alternative method for determining the CSA has to be used. An appropriate alternative is the following: 1) as shown in Figure 10(c), project the effective antennas onto a unit sphere centered on the point radiator; 2) calculate the area of the sphere ($S_{\text{effective}}$) covered by the projections of the effective antennas. The projections of the antenna elements are unequally spaced and the spherical surface covered by them is irregular. A Monte Carlo method [31] is adopted in the second step to estimate the area. It can be easily proved that for a unit sphere, the CSA is simply given by $S_{\text{effective}}$.

Figure 11 shows the simulation results of the selected location on the shoulder as an example. The HPBW of the PSF in the normal and transverse directions can be obtianed from each PSF slice. The simulation results for locations A–G are summarized in Table 1. As is observed, the CSA of locations A and B, which are situated on the planar-like structure, is about 2π. The spatial resolution of these locations is approximately 9 mm and 5 mm in the normal and transverse directions, respectively. The CSA and spatial resolution of the locations C and D, which are situated on the cylindrical-like structures, are similar to that on the planar-like structures. But for locations E, F, and G, which are located on the concave-like structures, the CSA falls to 1.2π, 1.6π, and 1.4π, respectively. Meanwhile, compared with locations A to D, the spatial resolution is slightly degraded in both normal and transverse directions. The simulation results show that the spatial resolution is strongly related to the CSA of the location of

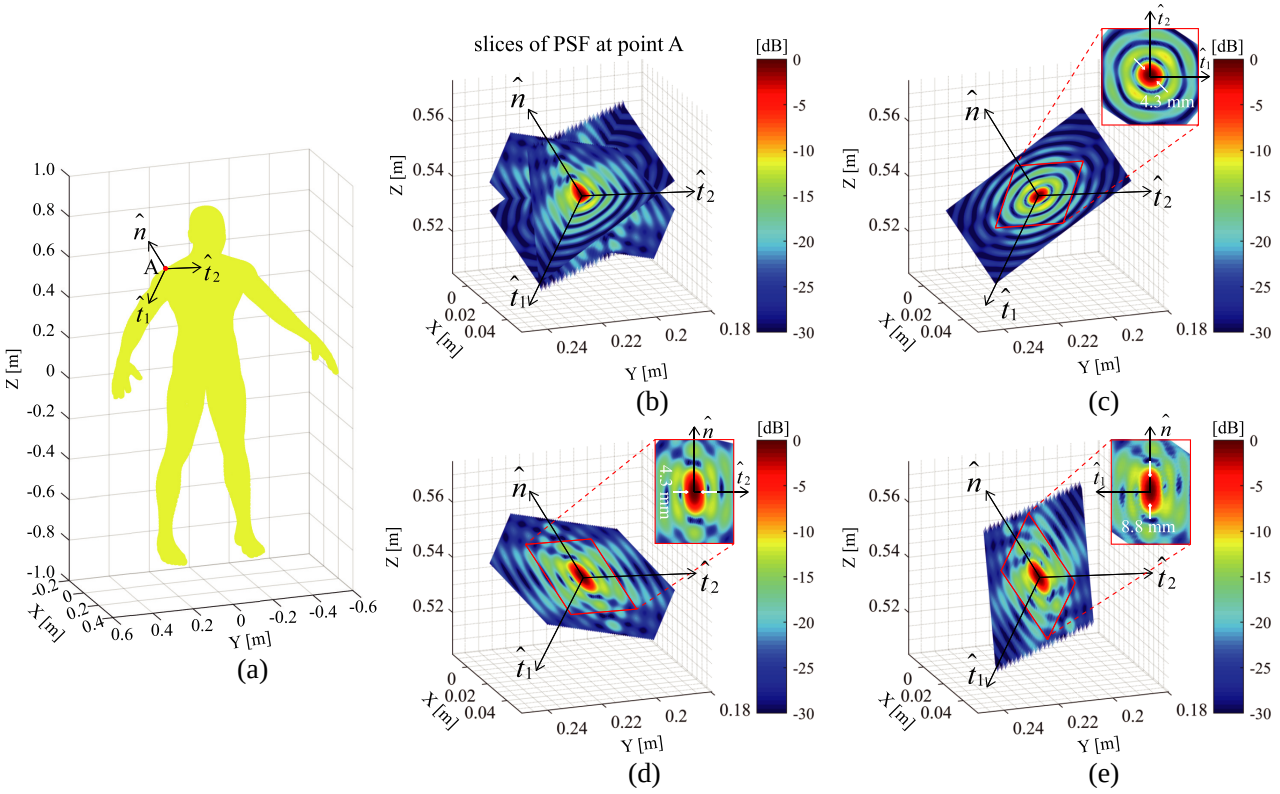

Figure 11. An example of a simulated PSF at the point A on the human body surface. (a) The human model illustrating the position of the point A. The red dot represents the selected point to set a Dirac delta function. The black arrows are the normal direction $\widehat{n}$ and transverse directions $\widehat{t}_1$ and $\widehat{t}_2$. (b) The PSF slices perpendicular to the normal and transverse directions. (c) The PSF slice parallel to $\widehat{t}_1$ and $\widehat{t}_2$. (d) The PSF slice parallel to $\widehat{n}$ and $\widehat{t}_2$. (e) The PSF slice parallel to $\widehat{n}$ and $\widehat{t}_1$.

Table 1. The CAS and simulated imaging spatial resolution at locations A–G on the human body surface considering the obscuration effects.

Locations on the human body surface	A	B	C	D	E	F	G
CSA (Ω)	1.91π	1.92π	1.98π	1.92π	1.15π	1.58π	1.35π
Normal direction spatial resolution [mm]	8.8	9.3	9.4	9.1	10.4	9.9	10.1
Transverse direction spatial resolution: long axis [mm]	4.6	4.6	4.6	4.6	7.3	4.7	4.9
Transverse direction spatial resolution: short axis [mm]	4.1	4.1	4.1	4.1	4.2	4.0	4.6
Transverse direction spatial resolution: average [mm]	4.3	4.4	4.4	4.4	5.8	4.4	4.7

the point radiator. For location E, which has the smallest CSA, the spatial resolution is approximately 10 mm and 6 mm in the normal and transverse directions, respectively.

For comparisons with experimental measurements, the best that can be achieved is with near-field (but not surround) imaging systems. In one of these systems [18], a 22 GHz aperture synthesis imager

having a 10 cm diameter antenna array, had its transverse and normal spatial resolutions measured to be λ and 7λ respectively, at a range of 10 cm from the array. In another hybrid imaging system with aperture synthesis in the vertical direction and phased array beam-forming in the horizontal direction, which was operated at 34 GHz and having an aperture of 35 mm(V) $\times$ 40.8 mm(H) [32], the angular resolution in the vertical direction is around 1° [33]. To be specific, the transverse spatial resolution was measured to be 2.15λ at a range of 1 m in front of the array and 6λ at a range of 3 m [33]. These measured resolutions are greater than those shown in the Table 1 because the antenna array is not subtending a sufficiently large solid angle at the measurement location to enable the Abbe microscope resolution limit of $\lambda/2$ to be approached. Future systems would endeavor to subtend greater solid angles, where the antenna array would begin to surround the subject under measurement.

By performing curve fitting on the imaging spatial resolution at the positions A–G and their corresponding CASs, two curves, as shown in Figure 12, can be obtained. The expressions for these two fitted curves are:

$$f_1(x) = -0.0158x^2 - 0.3526x + 11.8987 \tag{9a}$$

$$f_2(x) = 0.4592x^2 - 4.9997x + 17.8021 \tag{9b}$$

where x represents the CSA, and f_1, f_2 represent the imaging spatial resolutions in the normal direction and transverse direction, respectively. Compared with the curves shown in Figure 9, it can be observed that the transverse direction imaging resolution, which is calculated using the simplified obscuration effects' model proposed in Section 4, is consistent with the simulation results for different CSAs. However, in the normal direction, the estimated imaging resolution by the simplified model is slightly poorer than the simulation results, and the error between them gradually increases as the CSA decreases. This implies that when the CSA of the radiation source approaches 2π, the simplified obscuration model proposed in this paper can be used to estimate the imaging resolution of the radiation source well, both in the normal and transverse directions. However, when the CSA of the radiation source is far smaller than 2π, the estimated imaging resolution in the normal direction by the simplified obscuration model is significantly larger than the actual imaging resolution.

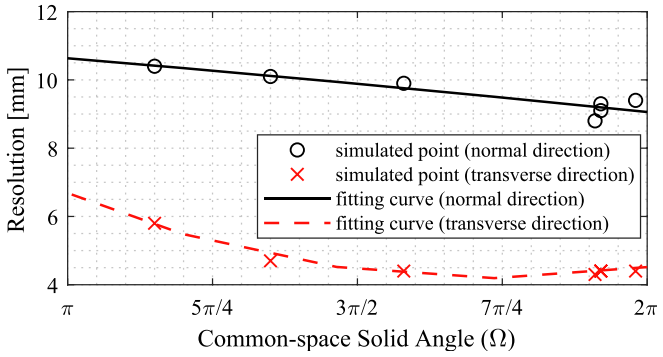

Figure 12. The variation curve of the imaging spatial resolution at the selected points in the normal and transverse directions as functions of the CSA.

By utilizing the simulation method proposed in this subsection, it is possible to compute the effective antennas, the CSA, and the passive 3-D imaging resolution for an arbitrary point source located on any surface. However, this process requires a considerable amount of computation. For instance, the human body model employed in this section is composed of around 100,000 facets, while the total number of receiving antennas is 5,000. Therefore, for a selected point source on the human body surface, at least 500 million calculations are required to determine whether there is an intersection point between the line connecting the radiation source and the receiving antenna and each facet. For the computer used in this work, equipped with an AMD Ryzen 5 3600X 6-Core processor having a clock speed of 3.8 GHz and 32 GB of random access memory (RAM), the total time required to compute the effective antennas and the CSA for a single point source is approximately 220 seconds.

5.2. 3-D Image Reconstruction of the Human Body Model

Results are now presented for the 3-D image reconstruction of the complete human body. A 3 meter diameter, 5000-antenna spherical array is used in the simulation to ensure a high quality reconstructed image. This first image is normalized and a thresholding process is applied. With a priori knowledge that the normalized intensity of the original human body model is 1, a threshold of 0.5 is selected to exclude the pixels whose normalized intensity is smaller than 0.5 and retain the pixels having a normalized intensity higher than 0.5, making the 3-D shape of the human body easily recognizable. According to the analysis in Section 3, the CSA of the point radiators on the human body is less than or equal to 2π. To reduce the number of numerical calculations, the CSA of every independent radiator is assumed to be 2π, this being sufficient to simulate the impact of the obscuration. On the contrary, the CSA is set to be 4π, to simulate the ideal case of no obscuration. To reduce computational complexity, a human body model consisting of 5105 facets is used for the passive 3-D image reconstruction in this subsection. As shown in (4), the calculation complexity of the image creation algorithm used in this paper is proportional to N^2. Table 2 displays the simulation time and computation resources for different numbers of array elements. Since the imaging algorithm operates in the spatial domain, using back-propagation, the image reconstruction time is the product of the imaging time of a single voxel and the required number of voxels in the image.

Table 2. The computer usage and simulation times vary greatly with the number of antenna elements in the array.

No. of antenna elements	200	300	500	1000	2000	5000
Visibility function generation time [s]	4.8	10.77	29.9	118.9	496	2997.3
Image reconstruction time of a single voxel [s]	0.003	0.007	0.015	0.039	0.15	0.69
Maximum CPU usage	60%	60%	60%	62%	71%	81%
Maximum RAM usage	40%	40%	40%	44%	48%	62%

Figure 13 demonstrates the comparison of the reconstructed 3-D images of the human body model with and without obscuration. The mean and standard deviation of the normalized intensity in Figure 13(a) (without obscuration) are about 0.95 and 0.01, respectively. Figure 13(b) indicates the mean and standard deviation (with obscuration) are 0.85 and 0.05, respectively. As shown in Figure 14, the maximum absolute deviation of the reconstructed 3-D images in Figures 13(a) and (b) is about 0.25 in both XOZ- and YOZ-slices. The mean and standard deviation of the absolute values of the deviations for the two 3-D images are 0.08 and 0.08, respectively. These simulation results indicate that the obscuration effects might cause a deterioration of the temperature resolution in the reconstructed 3-D image. It means that weapons or contraband detection may fail if the detection process is only dependent on image contrast, as there would be no means to discriminate threat objects from the background. It should be noted that in the simulations in this section, the CSA of all radiation sources is set to 2π. Therefore, in the reconstructed images shown in Figure 13(b), the regions suffering more severe obscuration effects, such as the armpits and between legs, do not show a significant decrease in the reconstructed normalized intensity. However, in practice, the reconstructed brightness temperature in these regions will be significantly lower than in other positions.

To simulate the scenario where the concealed object has a similar brightness temperature to the human body, the normalized intensity of the human body and a concealed gun are set as 1 and 0.9, respectively. Figure 15 shows the original model and the reconstructed 3-D image of a man carrying a gun. It is observed in Figure 15(b) that the reconstructed normalized intensity deviation between the gun and the human body is relatively small and the gun is hard to recognize from the intensity difference alone. However, the 3-D shape of the gun is still recognisable, despite the low contrast. Therefore, even if the obscuration effects may lead to a decrease of the temperature resolution in the reconstructed 3-D image, the detection of concealed objects can still be achieved through the 3-D shape recognition.

The analysis in Section 4 and simulation results in this section show that the simplified obscuration model proposed in Section 3 can to some extent reflect how the obscuration effects affect the spatial

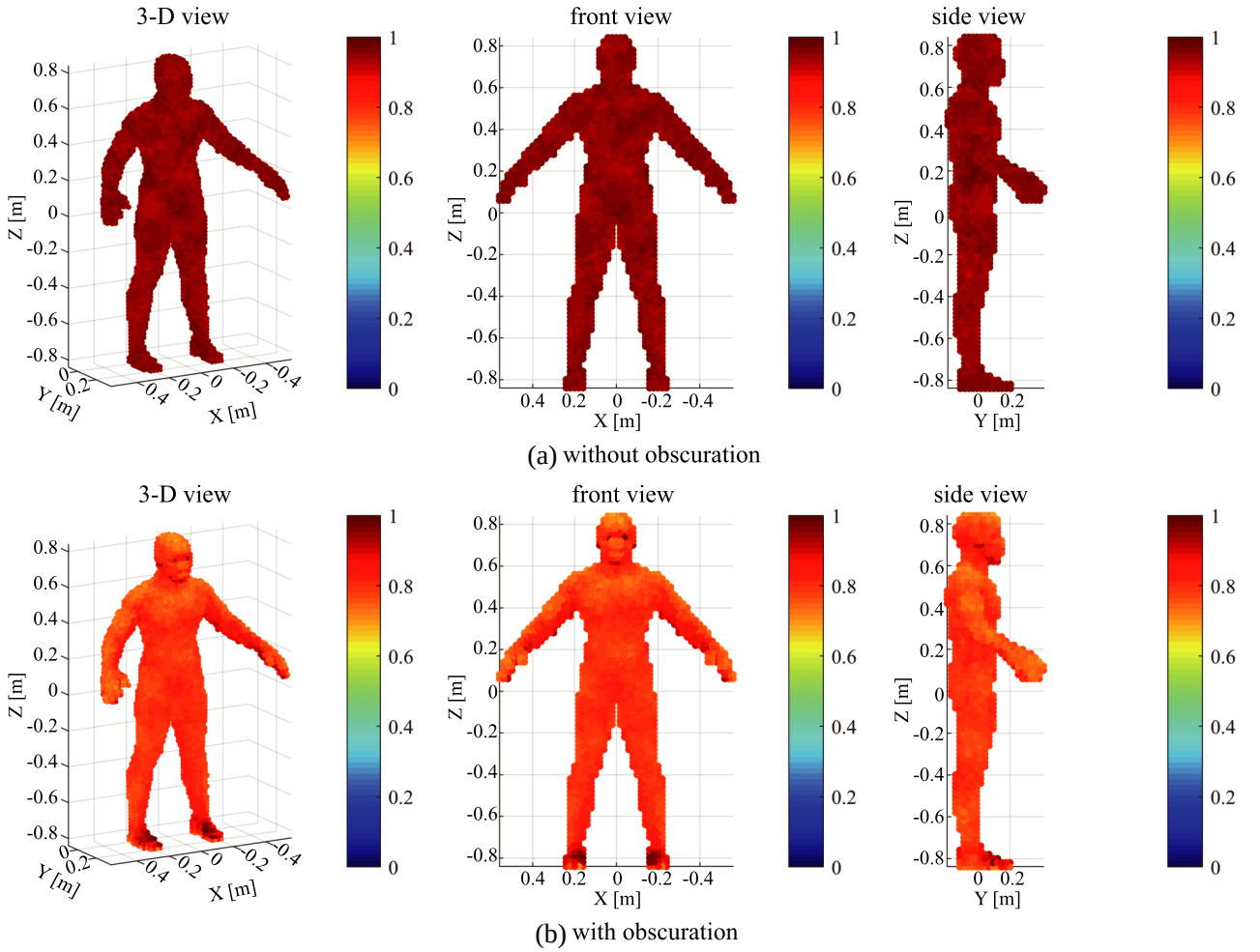

Figure 13. Comparison of the reconstructed 3-D images of the human body model without and with obscuration. The reconstructed 3-D images on the surface of the human body are shown for a CSA (Ω) of (a) 4π (without obscuration) and (b) 2π (with obscuration).

resolution of near-field passive 3-D imaging. To be specific, the obscuration effects cause changes in the CSA corresponding to the radiation sources at different positions, resulting in the radiation signals at different positions being received by a subset of antennas in the full array, this subset being referred to as the effective antennas. This means that the sampling baselines are distributed within a limited spatial frequency range, ultimately leading to differences in the imaging resolution at different locations on the human body surface. Furthermore, with the help of the proposed simplified model, this work reveals that the PSF and the imaging resolution are related to the shape of the source in the near-field passive 3-D imager. This is different from the traditional far-field imaging, where the PSF is usually considered to depend only on the imaging system and is independent of the source itself. Based on the proposed simplified model and simulation results, it is concluded that in near-field passive 3-D imaging, the achievable imaging spatial resolution has some dependency on the shape of the subject being imaged. This effect is more significant for the spatial resolution in the direction normal to the surface of the subject. Although the simplified model proposed in this paper cannot perfectly simulate the real measurement scenario, it can estimate the theoretical imaging performance of the human body to first order. As the effectiveness of using passive 3-D imaging technology for human security screening is still in its infancy, this work is of great significance for further verifying whether near-field passive 3-D imaging technology can be used by law enforcement agencies for the detection of prohibited items concealed on the human body.

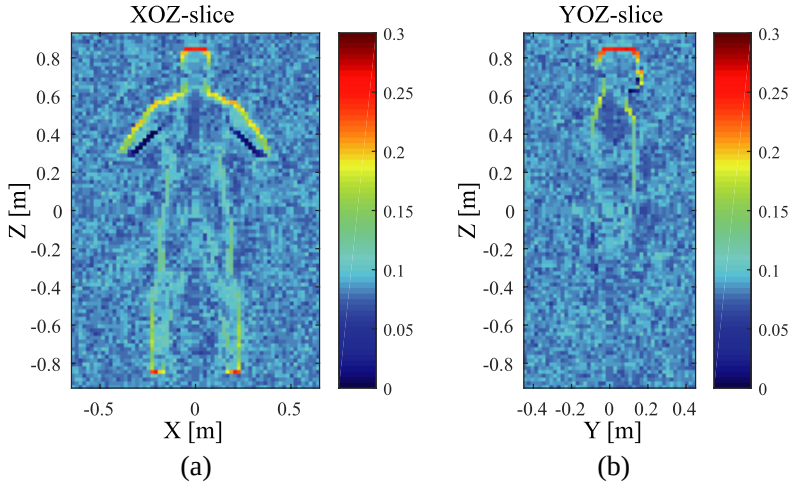

Figure 14. Absolute deviations of the reconstructed brightness temperatures in Figure 13 are shown through the 3-D image in the (a) X-Z plane, (b) the Y-Z plane. The deviations indicate the errors arising in the brightness temperature reconstructions in moving from an $\Omega = 4\pi$, to an $\Omega = 2\pi$ obscuration.

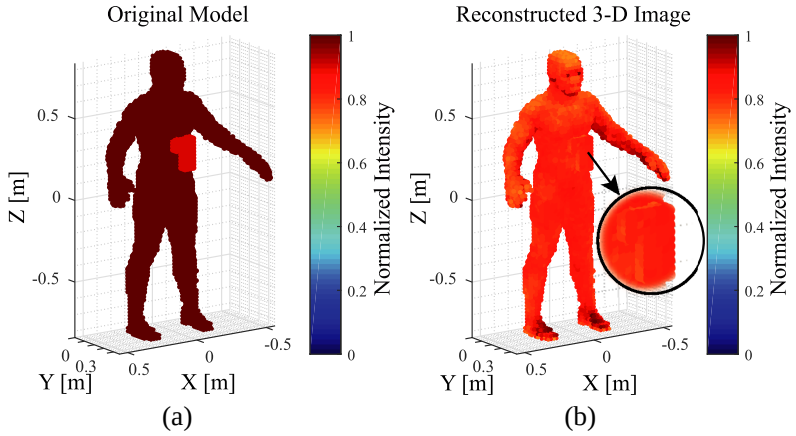

Figure 15. The reconstructed 3-D images of a human model carrying a gun: (a) the original model of a human body carrying a gun, with a normalized intensity of 1 and 0.9, respectively; (b) the reconstructed 3-D image.

6. DISCUSSION

In Section 4 and Section 5, the 500-element and 5000-element arrays are used to simulate the imager performance. The choice of the number of antenna elements will certainly affect the imaging quality. Furthermore, considering the obscuration effects, the number of effective antennas decreases as the CSA decrease. The reduction in the number of effective antennas might also cause degradation in the spatial resolution of the reconstructed 3-D image. For these reasons, a comparison of the PSF of the 500-element and 5000-element evenly spaced spherical arrays will now follow. Future work will also be discussed in this section.

6.1. Impact of the Number of Antenna Elements

For the ideal case, all of the antenna elements in the imager are effective antennas. When the point radiator is placed at the center of the array, the normal direction of the point radiator (0,0,1) becomes aligned with the $+Z$-axis. This enables the PSF of the 500-element and 5000-element arrays to be

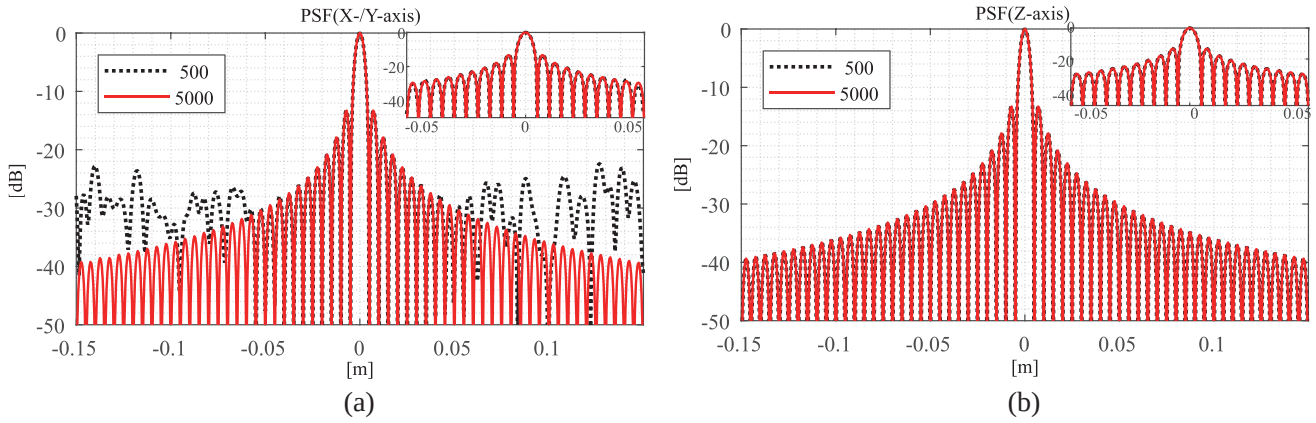

Figure 16. The PSFs of a 500-element and a 5000-element antenna spherical array, shown along: (a) the X- and Y-axes (the transverse direction) and (b) the Z-axis (the normal direction).

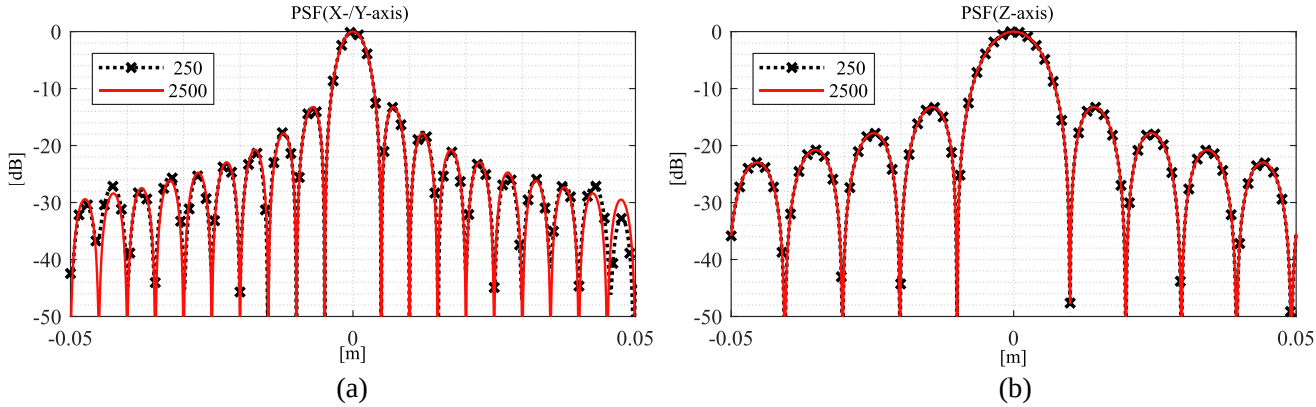

Figure 17. For comparison, the PSFs of the 500-element and 5000-element antenna array for a CSA of 2π (the effective number of antennas being 250 and 2500, respectively), are shown: (a) along the X- and Y-axes (the transverse direction); (b) along the Z-axis (the normal direction).

calculated.

Figure 16 shows the comparison of the PSF of the 500-element and 5000-element array along the X-, Y-, and Z-axes. It is observed that the HPBWs of these two arrays are the same in the three axes. It means that the two arrays have the same imaging spatial resolution. However, the mean sidelobe intensities in the X-axis and Y-axis directions of the PSF of the 500-element array are higher than that of the 5000-element array. This indicates that the 5000-element array has a higher main beam efficiency, which will result in better imaging quality. The asymmetry of the sampling points of the PSF along the X- (or Y-) and Z-axes is due to the antenna array not being perfectly symmetric.

In consideration of the obscuration effects, it is assumed that the CSA of the point radiator reduces from 4π to 2π. This is true provided that the antenna elements on the southern hemisphere are obscured, which is the case, as indicated in Figure 4(c) and Figure 8(b). This means the number of effective antennas of the 500-element array and 5000-element array becomes 250 and 2500, respectively, which is used below to estimate the performance.

Figure 17 illustrates a comparison of the PSF of the two antenna arrays having 250 and 2500 effective antennas. It is observed that the HPBWs of the PSF of the two arrays are the same in all three axes. It means that this change in effective antenna numbers has little effect on the imaging spatial resolution. However, a further reduction in the CSA, below π, will affect the imaging spatial resolution.

In conclusion, spherically shaped imaging arrays with greater numbers of antenna elements can

deliver images of higher quality, but they have little effect on the imaging spatial resolution. Therefore, in order to exclude the influence of the number of antenna elements on the simulation results, this study uses an imaging array having the largest number of antennas possible, within the limits of reasonable computation times, this number being 5000.

6.2. Future Work

With the theoretical achievable imaging resolution in 3-D imaging proven and the opportunities for 3-D optical cameras to augment the image creation algorithms highlighted, considerations are now made about future developments that would enable the realisation of 3-D mm-wave aperture synthesis security screening portals. Three areas are now proposed for further research, namely, refinements to the scene simulation model, faster 3-D image creation and analysis algorithms and the development of optimal antenna array topologies.

6.2.1. Refinements to the Scene Simulation Model

The scene simulation method utilized in this paper has simplified the actual imaging scenarios and disregarded various influential factors present in the real world. Apart from the radiometric emission received directly from the human body, there is additional emission received from the environment by reflection from the human body. Although the level of any multiply reflected environmental radiation may be minimal in an outdoor environment, or brought to a deterministic level indoor by the use of millimeter-wave absorber, this reflected radiation has not been considered in the model. In a more refined simulation model, multiple reflections may be taken into account, together with back-face culling in the ray-tracing. These are well established techniques from computer graphics and have been used in a small number of scenarios [9, 34] for passive imaging, but not for aperture synthesis. This would estimate more precisely the visibility function of aperture synthesis of the human body, upon which the whole imaging technique is dependent. This more refined model would not only model the reflections from the environment, but also model the obscuration effects of parts of the body directly, without the need for assumptions about the CSA for different body regions. This however is a considerable increase in the level of sophistication of the model and would undoubtedly require greater computational resources. Nevertheless, it is earmarked for future work and for experimental validation, so a highly reliable model is available to assess system performances in novel security screening scenarios.

6.2.2. Faster 3-D Imaging Creation and Analysis Algorithms

The imaging algorithm used in this study is one of back-propagation in the spatial domain. With the sacrifice of computational efficiency, this imaging algorithm has the benefits of excellent and uncompromised imaging performance, and wide FOVs. This is a powerful tool to explore the theoretical limits of 3-D aperture synthesis image creation in security screening. However, the technique is computationally intensive and even with graphical processing units (GPUs), it is unlikely to be a route to real-time imaging. Real-time image creation and analysis is a necessity for security screening, so as not to stem the flow of traffic at airports and transport networks. A more efficient 3-D image creation algorithm for security screening is therefore sought. The 3-D images then need to pass through machine recognition algorithms to recognise threats rapidly from their 3-D shape.

6.2.3. Development of Optimal Antenna Array Topologies

A practical antenna array for passive 3-D imaging for human security screening must be one which samples the baselines of the radiometric field without redundancy and with as smaller number of elements as possible, thereby satisfying market requirements of performance and cost. The benefits and design of optimal 2-D antenna arrays for aperture synthesis in the field of astronomy has been discussed at length in [35]. Herein, these arrays have been referred to as non-redundant, as ideally no baseline is sampled more than once, this being considered inefficient and wasteful of hardware resources. In practice, no 2-D arrays exist that sample exactly all baselines only once. The best that can be achieved are arrays that sample each baseline only once, or a small number of times, these being referred to as

minimally redundant arrays. The potential task therefore arises, if and how a minimally redundant 3-D array operating in the near-field for 3-D imaging may be constructed. Building on the techniques used for 2-D arrays, identification of 3-D minimally redundant arrays would be through trial and error methods or nonlinear relaxation techniques, such as simulated annealing [36]. The antenna array needs to capture emission from all human body surfaces, so there are no areas of the human body which are hidden from measurement. Potentially an L-shaped array in a short walk-way would offer the possibility of measuring the front, back and sides of the human body, with antennas above and below to measure the head, tops of shoulders and between the legs of the body. Such an array would minimise effects associated with the obscuration discussed in this paper. The array would be conformally deployable on surfaces of opportunity at security screening locations and compatible with low-cost manufacturing techniques.

7. CONCLUSIONS

A model of obscuration effects in 3-D passive aperture synthesis imaging is presented and used by simulation to show how the PSF of the imager is related to the specific regions of the body being screened. The herein described method considers how limbs of the body, and the body shape, can reduce the solid angle over which radiometric emission can be measured by the imaging array that surrounds the body. In this novel application, the PSF becomes a function, albeit a weak one, of the object being imaged. This is in contrast to the usual situation, where the PSF is only a function of the optical system. The simulation results demonstrate that the major influence of the obscuration effects is on the degradation of spatial resolution in the direction normal to the human body surface. It is also shown how the imaging spatial resolution can be quantified in terms of a so-called Common-space Solid Angle, this being related to the level of obscuration set by the human body itself. The simulation results indicate that the spatial resolution over the majority of the human body surfaces is λ (10 mm@30 GHz) and $\lambda/2$ (5 mm@30 GHz) in the normal and transverse directions to the human body surface, respectively. In regions of the body where there are the highest levels of obscuration, such as in the armpits, the normal and transverse spatial resolutions may fall to λ (10 mm@30 GHz) and 5λ (50 mm@30 GHz) respectively. It is also shown how the quality of an image reproduced using the aperture synthesis imaging algorithms changes in going from that which offers the best possible performance ($\geq$ 5000 antennas) to that of a more manageable number, from a cost perspective of 500. Possible future directions for research are discussed that would enable the realisation of 3-D aperture synthesis imaging for security screening of people.

ACKNOWLEDGMENT

The authors would like to acknowledge the support of this research from the National Natural Science Foundation of China (Grants No. 61731001 and No. 62171011) and to thank Weikang Si and Dongrong Zhang of Beihang University for their suggestions on the writing of this paper.

REFERENCES

1. Luukanen, A., R. Appleby, M. Kemp, and N. A. Salmon, "Millimeter-wave and terahertz imaging in security applications," *Terahertz Spectroscopy and Imaging*, Springer Berlin Heidelberg, 2013.
2. Nanzer, J. A., *Microwave and Millimeter-wave Remote Sensing for Security Applications*, Artech, 2012.
3. Ahmed, S. S., "Microwave imaging in security — Two decades of innovation," *IEEE Journal of Microwaves*, Vol. 1, No. 1, 191–201, 2021.
4. Martin, C. A. and V. G. Kolinko, "Concealed weapons detection with an improved passive millimeter-wave imager," *Proc. SPIE — The International Society for Optical Engineering*, Vol. 5410, 252–259, 2004.

5. Salmon, N. A., R. Macpherson, A. Harvey, P. Hall, S. Hayward, P. Wilkinson, and C. Taylor, "First video rate imagery from a 32-channel 22-GHz aperture synthesis passive millimetre wave imager," *Proc. SPIE — Millimetre Wave and Terahertz Sensors and Technology IV*, Vol. 8188, 31–42, 2011.
6. Hu, T., Z. Xiao, H. Li, R. Lv, and X. Lu, "Experimental methods of indoor millimeter-wave radiometric imaging for personnel concealed contraband detection," *Proc. SPIE — The International Society for Optical Engineering*, Vol. 9275, 201–209, 2014.
7. Zheng, C., X. Yao, A. Hu, and J. Miao, "A passive millimeter-wave imager used for concealed weapon detection," *Progress In Electromagnetics Research B*, Vol. 46, 379–397, 2012.
8. Heinz, E., T. May, D. Born, G. Zieger, S. Anders, V. Zakosarenko, H. G. Meyer, and C. Schäffel, "Passive 350 GHz video imaging systems for security applications," *J. Infrared, Millimeter, Terahertz Waves*, Vol. 36, No. 10, 879–895, 2015.
9. Salmon, N. A., "Indoor full-body security screening: Radiometric microwave imaging phenomenology and polarimetric scene simulation," *IEEE Access*, Vol. 8, 144621–144637, 2020.
10. Coward, P. R. and R. Appleby, "Development of an illumination chamber for indoor millimeter-wave imaging," *Proc. SPIE — Passive Millimeter-Wave Imaging Technology VI and Radar Sensor Technology VII*, Vol. 5077, 54–61, 2003.
11. Doyle, R., B. Lyons, A. Lettington, T. McEnroe, J. Walshe, J. McNaboe, and P. Curtin, "Illumination strategies to achieve effective indoor millimeter wave imaging for personnel screening applications," *Proc. SPIE — Passive Millimeter-Wave Imaging Technology VIII*, Vol. 5789, 101–108, 2005.
12. Thompson, A. R., J. M. Moran, and G. W. Swenson, *Interferometry and Synthesis in Radio Astronomy*, Springer, Cham, 2017.
13. Zheng, C., X. Yao, A. Hu, and J. Miao, "Initial results of a passive millimeter-wave imager used for concealed weapon detection BHU-2D-U," *Progress In Electromagnetics Research C*, Vol. 43, 151–163, 2013.
14. Zhao, Y., A. Hu, W. Si, X. Guo, and J. Miao, "Calibration of visibility samples for real-time passive millimeter wave imaging," *IEEE Access*, Vol. 9, 106441–106450, 2021.
15. Salmon, N. A. and N. Bowring, "Near-field and three-dimensional aperture synthesis imaging," *Proc. SPIE — Millimetre Wave and Terahertz Sensors and Technology VI*, Vol. 8900, 109–117, 2013.
16. Salmon, N. A. and N. Bowring, "Three-dimensional radiometric aperture synthesis microscopy for security screening," *Proc. SPIE — Millimetre Wave and Terahertz Sensors and Technology VII*, Vol. 9252, 12–20, 2014.
17. Salmon, N. A. and N. Bowring, "Simulations of three-dimensional radiometric imaging of extended sources in a security screening portal," *Proc. SPIE — Millimetre Wave and Terahertz Sensors and Technology VIII*, Vol. 9651, 965106, 2015.
18. Salmon, N. A., "3-D radiometric aperture synthesis imaging," *IEEE Trans. Microwave Theory Tech.*, Vol. 63, No. 11, 3579–3587, 2015.
19. Goodman, J. W., *Statistical Optics*, Wiley, America, 2015.
20. Salmon, N. A., "Spatial resolutions and field-of-views in millimetre wave aperture synthesis security screening imagers," *Proc. SPIE — Millimetre Wave and Terahertz Sensors and Technology XI*, Vol. 10800, 1080004, 2018.
21. Lipson, A., S. G. Lipson, and H. Lipson, *Optical Physics*, Cambridge University Press, New York, 2010.
22. Zhang, Z., *Microwave Radiometry Technology and Application*, Beijing Publishing House of Electronics Industry, Beijing, 1995.
23. Camps Carmona, A. J., *Application of Interferometric Radiometry to Earth Observation*, Universitat Politècnica de Catalunya, 1996.
24. Corbella, I., N. Duffo, M. Vall-Llossera, A. Camps, and F. Torres, "The visibility function in interferometric aperture synthesis radiometry," *IEEE Trans. Geosci. Electron.*, Vol. 42, No. 8, 1677–1682, 2004.

25. Carter, W. H., "Three different kinds of fraunhofer approximations. II. Propagation of the cross-spectral density function," *J. Mod. Opt.*, Vol. 37, No. 1, 109–120, 1990.
26. Carter, W. H., "On refocusing a radio telescope to image sources in the near field of the antenna array," *IEEE Trans. Antennas Propag.*, Vol. 37, No. 3, 314–319, 1989.
27. Peichl, M., H. Suess, M. Suess, and S. Kern, "Microwave imaging of the brightness temperature distribution of extended areas in the near and far field using two-dimensional aperture synthesis with high spatial resolution," *Radio Sci.*, Vol. 33, No. 3, 781–801, 1998.
28. González, Á., "Measurement of areas on a sphere using Fibonacci and latitude-longitude lattices," *Math. Geosci.*, Vol. 42, No. 1, 49–64, 2010.
29. "MakeHuman: Open Source tool for making 3D characters," http://www.makehumancommunity.org.
30. Salmon, N. A., "Outdoor passive millimeter-wave imaging: Phenomenology and scene simulation," *IEEE Trans. Antennas Propag.*, Vol. 66, No. 2, 897–908, 2017.
31. Rubinstein, R. Y. and D. P. Kroese, *Simulation and the Monte Carlo Method*, Wiley, New York, 2016.
32. Zhao, Y., W. Si, B. Han, Z. Yang, A. Hu, and J. Miao, *IEEE Access*, Vol. 10, 32879–32888, 2022.
33. Chen, X., A. Hu, J. Gong, and J. Miao, "Ka band low channel mutual coupling integrated packaged phased array receiver front-end for passive millimeter-wave imaging," *Micromachines*, Vol. 14, No. 4, 2023.
34. Salmon, N. A., "Polarimetric scene simulation in millimeter-wave radiometric imaging," *Proc. SPIE — Radar Sensor Technology VIII and Passive Millimeter-Wave Imaging Technology VII*, Vol. 5410, 260–269, 2004.
35. Kopilovich, L. and L. Sodin, "Multielement system design in astronomy and radio science," *Springer Science + Business Media B.V.*, 2001.
36. Ruf, S. C., "Numerical annealing of low-redundancy linear arrays," *IEEE Trans. Antennas Propag.*, Vol. 41, No. 1, 85–90, 1993.